Characterization of the spherulitic deformation in equatorial region and cavitation in HDPE materials submitted to mixed-mode oligo-cyclic tensile loading

Hang Guo, R.G. Rinaldi, Sourour Tayakout, Morgane Broudin, Olivier Lame

Version of Record: https://www.sciencedirect.com/science/article/pii/S0142941821001586
Manuscript_7879b96a143e51508804768f60eecec8

Characterization of the spherulitic deformation in equatorial region and cavitation in HDPE materials submitted to mixed-mode oligo-cyclic tensile loading

Hang GUO[1], Renaud G. RINALDI[1], Sourour TAYAKOUT[2], Morgane BROUDIN[3], Olivier LAME[1*]

[1]MATEIS-CNRS UMR5510, Bat. Blaise Pascal, INSA-Lyon, F-69621, Villeurbanne, France

[2]EDF-DIPNN-Direction Technique, 19 rue Pierre Bourdeix, F-69007, LYON, France

[3]EDF-R&D Lab Les Renardières, Avenue des Renardières-Ecuelles, F-77250, Moret-Loing-et-Orvanne, France

*Corresponding authors: Olivier LAME
E-mail: olivier.lame@insa-lyon.fr

Abstract

The characterization of the mechanical response of semi-crystalline high-density polyethylene (HDPE) materials submitted to mixed mode oligo-cyclic tensile loading condition is attempted. More precisely, HDPE materials of varying microstructures triggered via thermal treatments, are cycled to a prescribed strain in the vicinity yet beyond the elastic limit and then retracted to zero stress. Macroscopically, a Mullins-like effect can be observed. At the meso- and micro- scales, in-situ SAXS measurements have been carried out so that the local deformation of the equatorial region of the spherulites can be estimated along with the broad evolutions of the crystalline spherulitic structures and the cavitation. Upon loading, the local strain is found proportional to the macroscopic one in the equatorial region of the spherulites. The shearing of the crystallites initiates during the first cycle and slightly accumulates with increasing cycles. Moreover, nano-sized cavities are only observed in the isothermal samples exhibiting higher crystallinity and a lower density of stress transmitters. These micro-voids are nucleated during the first loading step. Assuming that the cavities do not merge, it is found that the accumulation-saturation of the cavity volume fraction is essentially resulting from their dimension increase, especially along the direction perpendicular to the macroscopic elongation.

Keywords: semi-crystalline polymers; oligo-cyclic tensile loading condition; in-situ SAXS measurements; cavitation; spherulite

Introduction

High-density polyethylene (HDPE) are often shaped to produce pipelines, since high ductility is pursued to sustain potential seismic activity[1–3]. The investigation of the materials performance under seismic episodes for industrial applications is thus of strong interest. Oligo-cyclic tests with large stress/strain (beyond the elastic limit) and limited number of cycles are commonly set to model seismic events and have been widely performed onto various materials[4–6]. Ultimately, it is worth investigating the corresponding microstructure evolution and the associated mechanisms induced in order to better anticipate the materials responses to potential seismic events and predict its lifetime.

In this work, special attention is paid to tensile loading. The stress-controlled cyclic tests[7–10] can induce only limited plasticity per cycle, the maximum applied strain cannot exceed the yield point due to the further softening effect associated with necking initiation. Moreover, the strain-controlled tests (cyclic loading between two fixed strains) may cause potential compression/buckling, which is not desired. To avoid these disadvantages, the mixed-mode (oligo-) cyclic tensile loading is selected, the semi-crystalline polymer samples are stretched to a fixed strain and retracted to zero force repeatedly. With this multi-cycle test, *Mullins-like* effect including the progressive stress softening at maximum applied strain and the accumulation of residual strain at zero stress with increasing cycle number could be observed in the semi-crystalline polymers. The *so-called* Mullins phenomenon was firstly discovered in the filled and crystallizing rubbers[11–13] and further investigations proved that a similar phenomenon, at least its macroscopic manifestation, also prevails in semi-crystalline polymers[14–16]. Various authors suggested physical interpretations to the stress softening and accumulation of residual strain such as bond rupture[17], molecular slip[18], disentanglements[19] and network alteration theories[20]. some of them being mentioned for semi-crystalline polymers[14–16]. Nevertheless, the physical origins of this phenomenon are still controversial. However, based on the observations of *Mullins(-like)* effect, the first loading cycle leads to a “significant” structural evolution yet differing from the remaining cycles associated to its progressive accumulation.

The structural evolutions of polyethylene (PE) or other semi-crystalline polymers submitted to simple loading such as uniaxial tension have been widely studied at the meso- and micro- scales. At mesoscale, where the HDPE material can be depicted as a media of interconnecting spherulites, the deformation mechanisms were shown to be highly heterogeneous along the tensile direction[21–23]. In semi-crystalline polymers, authors made use of four critical strains to describe the tensile deformation of semi-crystalline polymers and the interplay between the elastic and plastic strain contributions[24,25]. The elastic deformation is classically assigned to

the amorphous phase and involves inter-lamellar separation, inter-lamellar shear and lamellar stack rotation[26,27]. During plastic deformation, various mechanisms may be involved, such as the shearing of the crystallites[27–33], cavitation[29,30,34–38], martensitic transformation[39,40] and fibrillation at large strain [41–43]. Among these, the cavitation and shearing of crystallites (also defined as the fragmentation of lamellae) are recognized as two competing mechanisms generated respectively in the crystalline and amorphous phases at small plastic strain ranges (in the vicinity of the neck initiation). The nucleation and growth of cavitation show a dependency on crystallization-related microstructural properties [44–46] such as the resulting thickness of crystalline lamellae and the density of stress transmitters (ST) including tie molecules and entanglements [29,30,47]. These elements play important roles in the

Several articles also discussed the microstructure evolutions in semi-crystalline polymers submitted to single loading-unloading path or fatigue tests. Focusing on cavitation, Addiego et al. have observed the partial reversibility of the cavitation in PE samples, distinguishing the total cavity volume fraction into a reversible part and a permanent part. The reversible contribution is further subdivided into an instantaneous elastic and a time-dependent viscoelastic one. Additionally, the permanent part depends on the applied strain level: for axial strain smaller than 4.1%, the cavities could be entirely reversible after relaxation[48]. Moreover, Raphael et al. reported the deformation and voiding of spherulitic microstructures in a pure polymer and glass-fiber reinforced polyamide 6.6 during fatigue tests by tomography analysis combined with SEM fractography observations[49]. In particular, they found that the cavity nucleation occurs firstly at equatorial plane of the spherulites, which is in accordance with the results reported by Mourglia-Seignobos et al. [9]. However, these classical fatigue tests are all conducted under stress-controlled loading conditions, and the imposed loading cycles (10^5-10^6 cycles) remain within the elastic regime. Moreover, Janssen et al. have reported that the failure mechanisms in the oligo-cyclic regime are different from the ones in high-cycle regime[8,50] in semi-crystalline polymers. Regarding the microstructure evolutions under mixed-mode cyclic conditions, beyond the elastic limit, only relevant studies performed on polymers other than semi-crystalline ones can be mentioned. Toki et al. performed a two-cycles *in-situ* SAXS/WAXS test to characterize the microstructure evolutions for a thermoplastic propylene-dominant ethylene-propylene copolymer. They noticed that the first cycle could destroy a fraction of the crystals and induce the reorientation of the other crystalline lamellae to form a "permanent set", which is thermally stable during the second loading[51].

The aim of this work is thus to further investigate the structural evolutions of semi-crystalline (HDPE) polymers under mixed-mode oligo-cyclic tensile loading conditions. Thermal treatments such as quenching and isothermal steps are applied to vary the initial microstructures, and *in-situ* SAXS measurements are performed to improve our understanding of the microstructural evolutions. Finally, the relation between the meso- and micro- structural evolutions and the aforementioned macro *Mullins-like* effect, if any, will also be discussed.

Experimental

Materials

Two types of commercial HDPE hereafter denoted as PE-A and PE-B are studied. These two materials were ordered from INEOS (Brussels, Belgium). It is worth noting that PE-B is a PE-100, widely used for tube applications, whereas PE-A is a HDPE for blow-molding applications. The two materials contain only minimal additives that are necessary for their shaping process: 1 to 1.5 g/kg of antioxidant and 1 g/kg of antacid. The two grades differ by their molecular topology and molar masses so that their microstructural and mechanical properties exhibit different sensitivity to thermal treatments. The molecular characteristics of the polyethylene pellets determined by gel permeation chromatography (GPC) are shown in **Table 1** (provided by INEOS Company).

Table 1: Molecular characteristics and isothermal treatment temperatures T_{iso} of PE pellets

Materials	M_n (g/mol)	M_w (g/mol)	M_z (g/mol)	T_{iso} (°C)
PE-A	7 500	202 200	1 478 900	121.5
PE-B	6 700	270 800	1 589 400	118

$M_{n,}$, M_w and M_z are the number-average molar mass, the weight-average molar mass and z-average molar mass measured by gel permeation chromatography.

Sample preparation

The PE pellets were molded at 200 °C for 10 min into 0.8 mm thick plates. Thermal treatments followed the compression molding step in order to modify the initial microstructure. On the one hand, plates were quenched in cold water and are further designated as “quenched” samples. On the other hand, some plates were wrapped and put into an oil bath at a constant temperature T_{iso} (shown in **Table 1**) for 17 h and are further defined as “isothermal” samples. The temperatures T_{iso} (121.5 °C and 118°C for PE-A and PE-B respectively) were chosen to meet two conditions: 1) the prescribed temperature should be close to the crystallization temperature so that the complete crystallization occur at a much lower rate[44,52]. 2) Furthermore, with this selected

temperature, the isothermal treatments could hinder secondary crystallization, which may have affected the materials mechanical properties[52].

DSC (Differential Scanning Calorimetry) analysis

6 to 8 mg samples cut from the molded plates were heated up to 150°C at a heating rate 10°C/min under nitrogen flow with a DSC 7 PerkinElmer apparatus, which has been indium-calibrated. Equation (1) below was used to determine the crystallinity (X_c) of the pristine samples:

$$\mathrm{X_c} = \frac{\Delta \mathrm{H_f}}{\Delta \mathrm{H_f^0}} \quad (1)$$

Where ΔH_f is the specific melting enthalpy and ΔH_f^0 is the melting enthalpy of a theoretically fully crystalline polyethylene. ΔH_f^0 was set equal to 290 J/g[53].

Tensile measurements

Tensile tests were conducted on dumbbell-shaped samples of 6.5 mm gauge length, 4 mm width and about 0.8 mm thickness. The specimen were punched from the processed plates then tested at room temperature (about 23°C) and a constant nominal strain rate of $\dot{\varepsilon} = 5 \times 10^{-2}\ \mathrm{s}^{-1}$ with a MTS 1/ME machine equipped with a 5KN load cell. Single loading steps up to large strain were performed to measure the neck width, determined as the difference in nominal strain between the threshold point of plasticity (where the nominal stress is about 80% of the -maximum- yield stress σ_y) and the beginning of the constant-stress neck propagation. This indicator is qualitatively related to the density of stress transmitters (ST) including tie molecules and entanglements. More specifically, the greater the nominal strain difference, the higher the ST density[54]. For each condition, at least three samples were tested and the results were averaged.

Mixed-mode oligo-cyclic tensile tests coupled with in-situ SAXS (Small-angle X-ray scattering) measurements

The small-angle X-ray scattering measurements were performed on the SWING beamline of the French SOLEIL synchrotron with a wavelength of 0.78Å. The beam size is 100×40 μm^2. The distance between the samples and the detector was 2.08m, so that the corresponding range of observation (scattering vector q) spans from 0.06 to 5.5nm^{-1}. The long period (L_p) was computed from a scattering vector q_{max} corresponding to the maximum Lorentz-corrected diffuse intensity using equation (2):

$$\mathrm{L_P} = \frac{2\pi}{\mathrm{q_{max}}} \quad (2)$$

It is worth noting that the Gaussian fit of the Iq^2-q profile in the vicinity of the peak was used to determine q_{max}. In addition, the thickness (L_c) of the spherulite crystalline lamellae was estimated as follow:

$$L_c = L_P \frac{\rho}{\rho_c} X_c \quad (3)$$

$$\frac{1}{\rho} = \frac{X_c}{\rho_c} + \frac{1-X_c}{\rho_a} \quad (4)$$

Where ρ, ρ_a, ρ_c are the overall sample, the amorphous phase (0.850 g/cm^3) and the crystalline phase (1.003 g/cm^3) densities respectively[55]. X_c is the crystallinity measured by DSC (see Equation 1).

A homemade miniature apparatus was used to conduct the mixed-mode oligo-cyclic tensile tests consisting in 8 consecutive cycles at constant nominal strain rate $\dot{\varepsilon}_{oc}=10^{-3}s^{-1}$. The maximum applied strain was ε_{oc}= 0.16, beyond the elastic limit. The 2D SAXS patterns were recorded every 30 s in real time. With these settings, the SAXS patterns were acquired every 0.003 increment in macroscopic nominal strain. Finally, these *in-situ* measurements were carried out on samples identical to those shaped for the tensile tests.

Results and analysis

Microstructure characterization of the pristine materials

Table 2 lists some physical characteristics (crystallinity X_c, long period L_p, thickness of crystallites L_c and neck width connected to the density of ST) of the pristine materials studied. It is worth noting that the precision of the neck width measurement did not allow differentiating the densities of ST between the PE-A and PE-B samples subjected to the same thermal treatment. Yet, **Figure 1** displays the nominal stress-strain tensile responses up to an axial nominal strain of 1 for the 4 materials in which the influence of the thermal treatments is clearly emphasized. In comparison to the quenching process, the isothermal treatment promotes the formation of relatively thicker crystalline lamellae as well as higher crystallinity and a lower density of ST [54]. It is worth noting that the effect of thermal treatment on the measured microstructure markers is consistent with former studies[21,22,29,30].

Table 2. Physical characteristics of the HDPE pristine microstructures.

Materials		X_c (%)	L_p (nm)	L_c (nm)	Neck width (-)
Experimental method		DSC	SAXS	SAXS	Tensile test
PE-A	Quenched	62.1	22	13	0.55

	Isotherm	73.4	35	24	0.30
PE-B	Quenched	57.7	20	11	0.50
	Isotherm	64.0	33	20	0.35

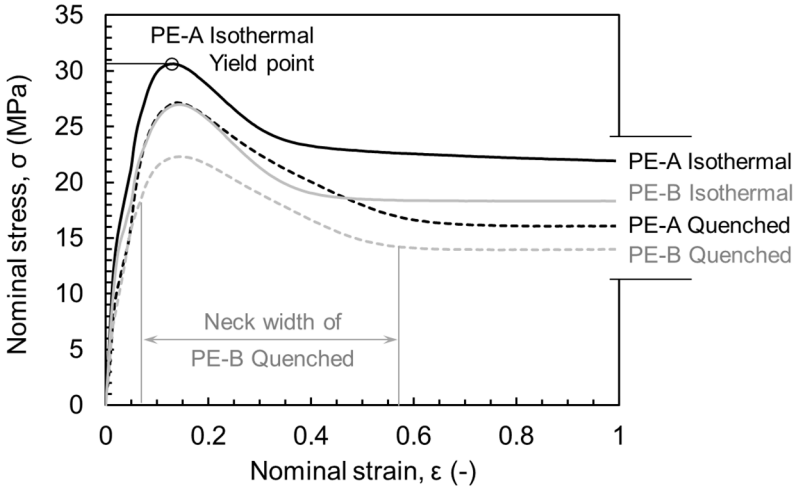

Figure 1 : Tensile curves and measurement of neck width

Structural evolutions of PE samples at different scales

The meso- and micro- structural evolutions of the HDPE samples submitted to mixed mode oligo-cyclic tests was evaluated by SAXS measurements. The 2D-SAXS patterns of either the two quenched or the two isothermal samples did reveal significant differences. Yet, few differences could be observed between the different HDPEs submitted to the same thermal treatment, hence suggesting similar "for the least qualitative" evolution. Consequently, the following focuses on the two PE-B materials (quenched and isothermal samples) and similar qualitative conclusions do apply for the PE-A materials. **Figure 2** presents the nominal stress-strain curves of the oligo-cyclic tests of the quenched (a) and isothermal (b) specimen respectively. It is worth noting that the loading path is seen to be stabilized after the 8th cycle. Therefore, only the first 8 cycles that involve the most significant evolutions (especially the first one) are investigated.

2D-SAXS patterns corresponding to five precise deformed states were added onto the figure (**Figure 2c**). Precisely, the pristine states, the maximum-strain and the zero-stress states of the 1st cycle and 8th cycle are displayed. For both samples, the 2D-SAXS patterns in the pristine state exhibit a circular ring suggesting that the lamellar stacks of spherulite are randomly oriented and that the material is isotropic.

For additional analysis, preferential directions that are parallel and perpendicular to the macroscopic loading direction are investigated and correspond respectively to the horizontal

(Zone H) and vertical (Zone V) regions of the 2D-SAXS patterns as evidenced onto the pristine image of PE-B Isothermal in **Figure 2c**. The azimuthal integrations are conducted with an angle of $\pm 5°$.

For quenched samples, with increasing strain during the first loading step, the ring-shaped pattern gradually becomes elliptical. The L_p at the equatorial region of the spherulite (corresponding to Zone H) increases upon stretching (the q-value decreases) as the equatorial crystalline lamellae of the spherulite are subjected to the local tensile load in the same direction as the macro sample and are thus pulled apart from one another. On the contrary, L_p at the pole (corresponding to Zone V) decreases (q-value increases) due to Poisson effect. When the applied strain reaches a critical value, the intensity in Zone H starts to decrease. Once unloaded to zero stress, the circular pattern is partly recovered and the scattering intensity of Zone H does not change significantly. At zero-stress states, the SAXS intensity of Zone H is seen to progressively decrease with increasing cycle number. Throughout the entire test, the evolution of the scattering intensity in the central part of the pattern is not remarkable meaning that the cavitation observed by SAXS is limited in these samples.

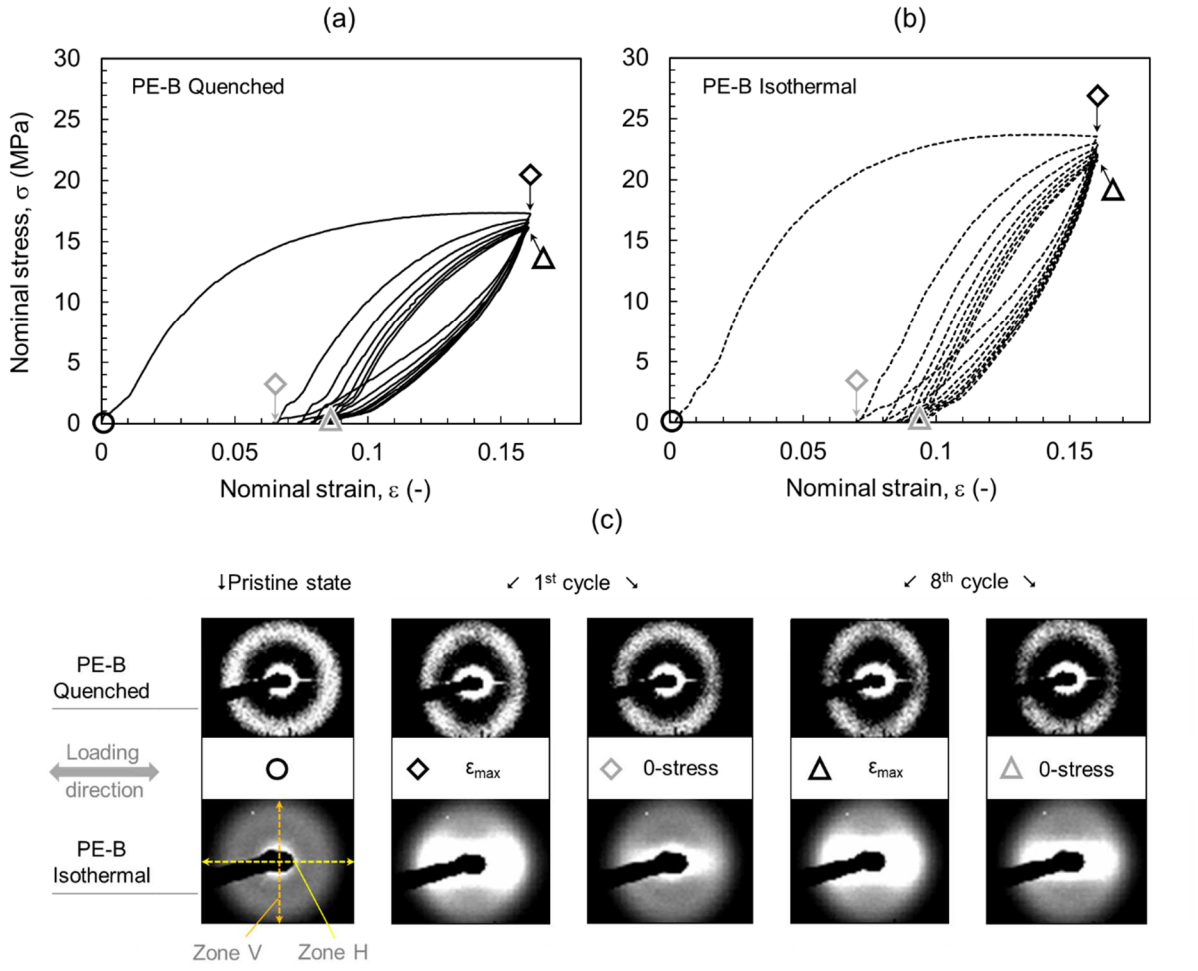

Figure 2: Evolution of the SAXS patterns during the oligo-cyclic tests for the PE-B samples:

(a) Quenched sample, (b) Isothermal sample. (c) 2D SAXS images for given deforming states (N.B. arbitrary gray scales).

For isothermal samples, the deformation of the spherulites as well as the deformation of the crystalline lamellae can hardly be discussed because of the strong intensity scattered by cavities. The cavitation appears during the first loading step in the vicinity of the yield point in the central part of the pattern. The strong intensity scattered is more elongated within Zone H, suggesting that the cavities are elliptical with its long axis being normal to the tensile direction[29,30]. Throughout a full cycle of load/unload, the cavity intensity and shape are naturally seen to change. The evolution appears to be more pronounced in the horizontal region (Zone H) with a distinct difference between the zero-stress 2D-SAXS patterns of the 1^{st} and 8^{th} cycle. Comparing the pattern after each cycle, the intensity scattered by cavities shows yet again an accumulating behavior.

Local deformation of spherulite

Addressing the local deformation of the spherulites is challenging due to their complex morphology and their dependency on the unknown local stress. In the equatorial region of the spherulite, the lamellar stacks are simplified as the flat-on sheets and assumed to have the same orientation: the norm of these lamellae is parallel to the tensile loading. During the tensile deformation, although the interlamellar amorphous phase is subjected to a triaxial stress[56], the local axial strain along the tensile direction in the equatorial region can be estimated by the spacing changes between these lamellae. It is of prime importance for further meso-macro modeling. The average spacing changes in the SAXS irradiated volume is evaluated with billions of lamellar stacks in the equatorial region. As a consequence, the data are believed to be representative of the considered deformed zone. Compared to the interlamellar separation (spacing changes of the lamellar stacks), the slight plastic deformation in the crystalline phase should be neglected in the equatorial region since the yield point has just been reached.

The spacing changes of the equatorial lamellar stacks could be computed using the azimuthal integrations of the equatorial region (Zone H). The corresponding Lorentz-corrected intensity profiles of the PE-B quenched sample, normalized by the thickness of samples, are presented in **Figure 3**.

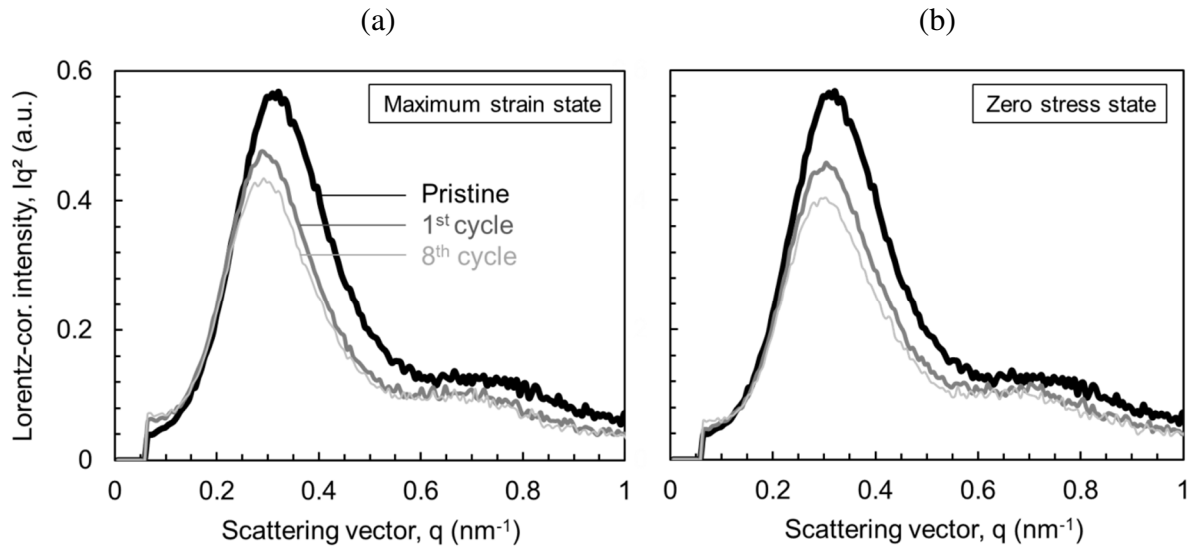

Figure 3: Equatorial Lorentz-corrected intensity as a function of q (PE-B Quenched samples) in the equatorial region (Zone H). (a) At maximum-strain state. (b) At zero-stress state.

The local strain at the equator of the spherulites could be calculated based on the evolution of the inter-lamellar long period L_p using relation (5):

$$\varepsilon_{local}(t) = \frac{\triangle L_p(t)}{L_{p0}} = \frac{L_p(t) - L_{p0}}{L_{p0}} \quad (5)$$

The end states of each cycle, corresponding to the maximum-strain (loading) and zero-stress (unloading) states are chosen to evaluate the relation between the local and the macroscopic strains. As previously discussed, the strong scattering intensity due to cavitation observed in the isothermal samples prevent the determination of L_p that is why only quenched samples are here studied. However, before the appearance of cavitation, the mechanisms leading to the deformation of the spherulites in both quenched and isothermal materials should be qualitatively similar[21,22]. **Figure 4a** illustrates the evolution of the local strain of the quenched samples as a function of cycle number. At maximum-strain states, both the macroscopic and the local strains remain mostly constant. Regarding the unloaded zero-stress states, both the macro and local residual strains exhibit an initiation-accumulation-stabilization behavior, and this spherulitic behavior is comparable to a Mullins-like phenomenon. The ratio of $\varepsilon_{local}/\varepsilon_{macro}$ at maximum-strain and minimum-stress states are plotted in **Figure 4b** as a function of cycle number. In both end states, a quasi-constant value of $\varepsilon_{local}/\varepsilon_{macro}$ of about 0.6 is observed, indicating that 1) the spherulitic deformation is directly (linearly) related to the macroscopic

axial deformation throughout the entire test, 2) heterogeneity exists at the microscale and that the equatorial region of the spherulites is less deformed than other regions along the macroscopic loading direction[21,22]. The fact that an almost constant ratio $\varepsilon_{local}/\varepsilon_{macro}$ is observed in the unloaded states suggests that no significant rupture in the spherulites occurs during the oligo-cyclic test performed.

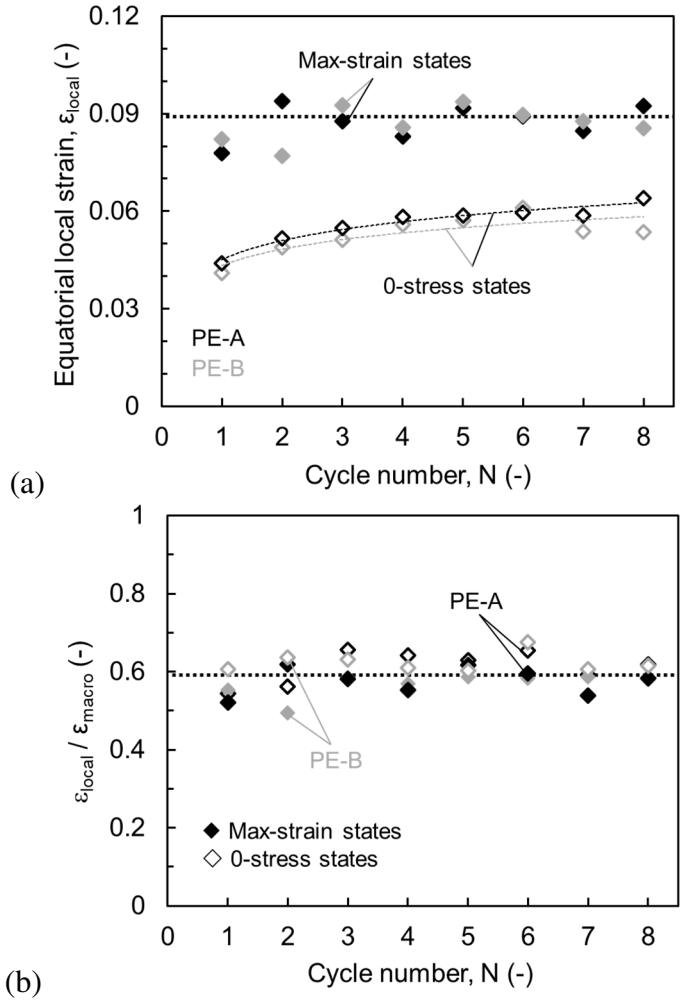

Figure 4: (a) Local strain at maximum-strain and minimum-stress states. (b) Plot of ratio $\varepsilon_{local}/\varepsilon_{macro}$ as a function of cycle number (quenched samples).

Evolution of the crystalline structure

Along with the spherulitic deformation, the crystalline structure of the spherulite also evolves. The structural alterations of the lamellar stacks are studied by monitoring the evolution of the intensity scattered $Q(\psi)$ that is defined as follow:

$$Q(\psi) = \int_0^\infty I^\psi(q)\, q^2 dq \qquad (6)$$

Where ψ is the azimuthal angle and $I^{\psi}(q)$ is the scattering intensity of the crystalline structure in the ψ direction normalized by the thickness of the sample. Assuming that the difference of electronic density remains constant, $Q(\psi)$ should be related to the volume fraction of oriented crystalline lamellae in the ψ direction[29,30].

The intensity scattered for 3 preferred azimuthal angles ψ=0° (equatorial region of the lamellar stacks), 90° (polar region of the lamellar stacks) and 45° (lamellar stacks oriented into 45° to the loading direction) are determined by azimuthal integration with $\Delta\psi$=±5°. Taking into account the finite experimental q-range covered, and using the onset (q_1) and end (q_2) of the peak of the scattering intensity of the crystalline structure as experimental limits, relation (6) can then be decomposed as follow:

$$Q(\psi) = \int_0^{q_1} I_1{}^{\psi}(q)\, q^2 dq + \int_{q_1}^{q_2} I_2{}^{\psi}(q)\, q^2 dq + \int_{q_2}^{\infty} I_3{}^{\psi}(q)\, q^2 dq \qquad (7)$$

In Equation 7 $I_2{}^{\psi}(q)$ is obtained experimentally for $q_1 \leq q \leq q_2$. $I_1{}^{\psi}(q)$ and $I_3{}^{\psi}(q)$ are extrapolated with a linear relation and the Porod's law respectively[29,30]. Finally, the evolution of the Q-value for the three preferred directions are presented in **Figure 5** as a function of time for the quenched samples. The evolution of the macroscopic axial strain with time is superimposed to better distinguish between the consecutive load/unload steps.

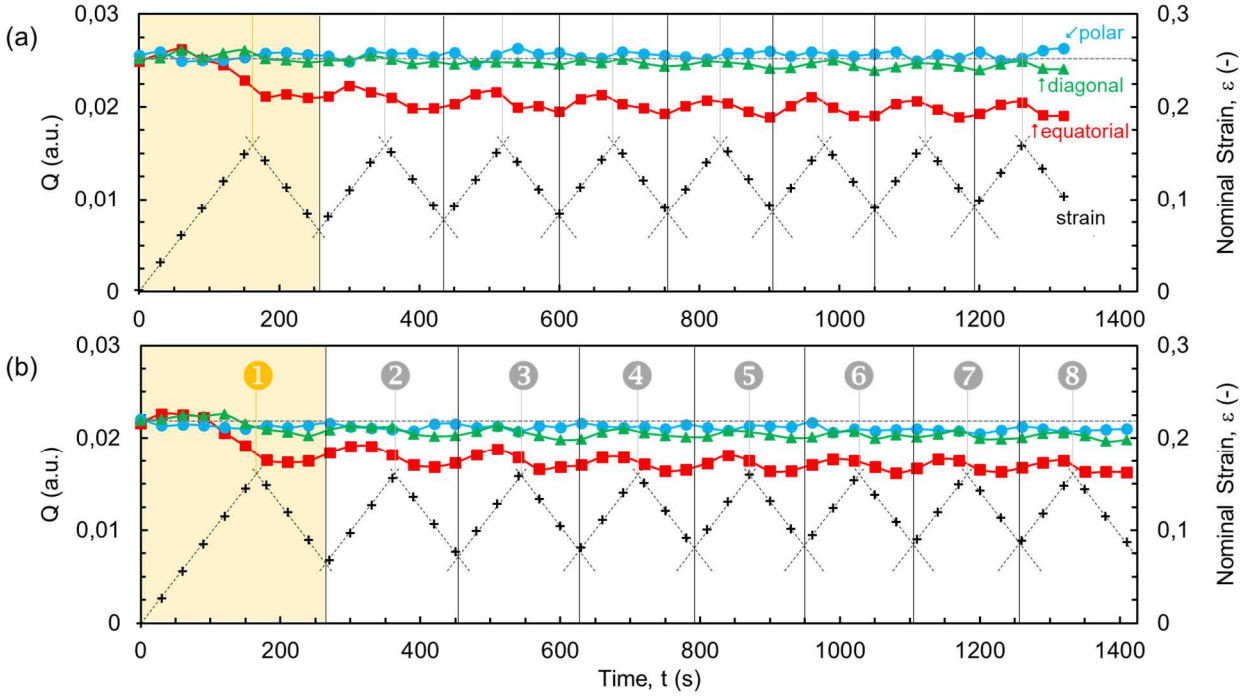

Figure 5: Evolution of Q value at different region of spherulite/applied macro-strain as a function of time: (a) PE-A Quenched sample; (b) PE-B Quenched sample.

For a given sample, the Q-value in the pristine state does not depend on the azimuthal angle which confirms the isotropy of the non-deformed state. During the deformation, the Q-values of the diagonal and polar regions do not exhibit an important variation, indicating that the local structures of the crystalline lamellae are i) not significantly modified and/or ii) sheared to large blocks with their orientation being nearly stable.

On the contrary, the Q-value focusing on the equatorial region of the spherulites evolves in an obvious periodic manner. During the first loading step, for macroscopic strain below the elastic limit ($\varepsilon \approx 0.1$), the Q-value scattered by the crystalline structure remains quasi-constant. Therefore, the spherulites are deformed with their lamellar structures being unaltered. For higher strain level, the scattering intensity begins to decrease, which means that the lamellar stacks at the equator are sheared or fragmented so that their preferential orientation (perpendicular to the tensile direction) is lost.

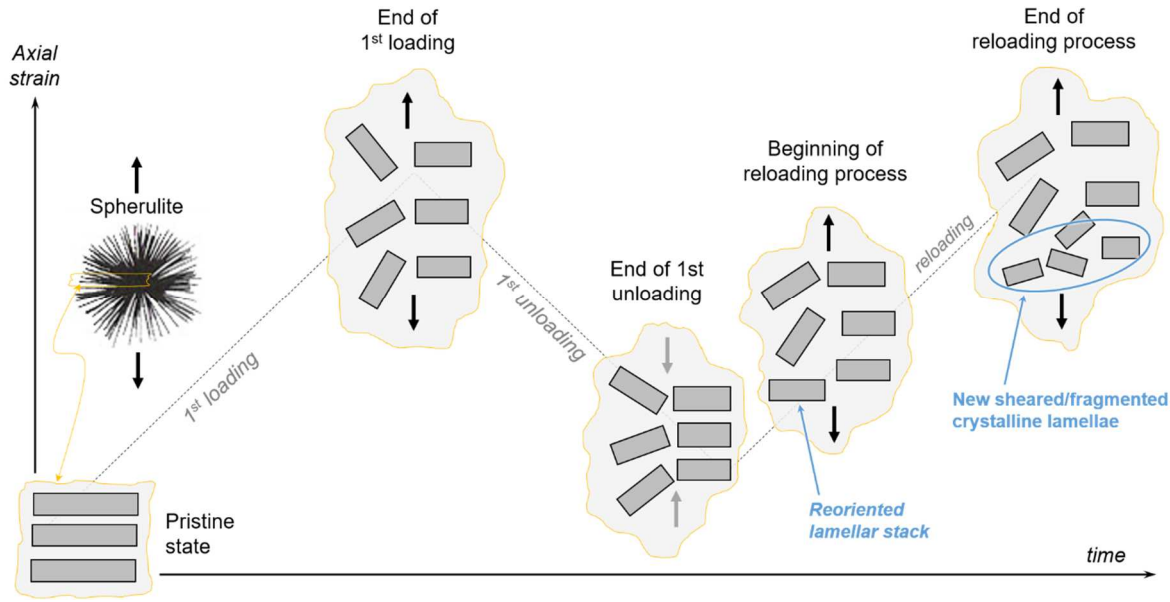

Figure 6: Evolution of the crystalline lamellae at the equator of the spherulite as function of oligo-cyclic loadings.

It is worth mentioning that these sheared/fragmented crystalline lamellae do not form highly oriented chevron structure manifested by a four-point diagram in 2D-SAXS patterns[57] which would result in the increase of the intensity at ψ=45° direction. During the unloading step, Q-value remains almost constant, suggesting that the orientation of the previously sheared/fragmented crystalline lamellae are still disordered. The following loading steps are quite different from the first cycle: in the early stage of the second loading, reorientation of a fraction of the sheared/fragmented crystalline lamellae at the equator where the chains tend to be

parallel to the tensile direction occurs. This phenomenon could lead to the increase of the *Q*-value. Nevertheless, the *Q*-value remains lower than its initial value, which means a large part of the previously sheared/fragmented lamellar stacks remains disordered. Moreover, as the strain overpasses a critical value, the *Q*-value begins to slightly decrease. This phenomenon is attributed to "weak" lamellar stacks that are sheared or fragmented. Throughout the consecutive deforming cycles, the scattering intensity of the equatorial region at the maximum-strain and zero-stress states first decreases then rapidly stabilizes. Finally, the schematic in **Figure 6** tends to summarize the evolution of the equatorial crystalline lamellae for representative states of the mixed-mode oligo-cyclic test.

Estimation of the observed cavity volume fraction and dissipation of energy due to cavities

Cavitation is an important micro-structural alteration also depicted as micro-damage that occurs in the amorphous phase of the polymer. In this work, the estimation of the cavitation volume fraction is based on an analytical method that has been initially proposed to calculate the volume fractions of a two-phase material with the aid to the equation (8).

$$2\pi^2\Delta\rho^2\Phi(1-\Phi)\mathrm{K}_1 = \int_0^\infty \mathrm{I(q)q^2\,dq} \tag{8}$$

I(q) is computed by azimuthal integration in the $0^\circ \leq \psi \leq 360^\circ$ range and corrected by the sample thickness. $\Delta\rho$ is the electronic density difference between the two phases, Φ is the volume fraction of one phase, and K_1 is an amplification factor. It is worth noting that K_1 depends on the level of deformation endured by the material. However, the account for this evolution should have limited effect on the estimation of the cavities volume fraction due to the high electronic density contrast between the cavitation and the dense polymer matrix. Therefore, K_1 is further set to be constant and only depends on the samples. Its estimation is obtained in the pristine state using equation (8). More precisely, considering that the materials are fully dense without appearance of cavities, the phases under considerations are the crystalline and the amorphous phases so that K_1 is the only unknown of the problem. Indeed, $\Delta\rho$ is the difference between the crystalline and the amorphous phase densities (ρ_c=1.003 g/cm^3 and ρ_a=0.853 g/cm^3 respectively[55]), Φ is the volume fraction of crystalline (or amorphous) phase, and the right end term is obtained using the method previously described and obtained using equation (7).
Under deformation, the two phases under considerations are now the HDPE matrix (as a whole) and the cavities. Consequently, $\Delta\rho$ is assimilated to the density of the PE sample ρ since the

density of the cavities is set to zero. It worth noting that this method only allows for the estimation of the volume fraction of the cavities that can be observed in the q-range of the SAXS measurement, later referred as V_{cav}^{SAXS}. However, this method provides a fair quantitative description of the evolution of the cavity volume fraction, which is representative and helpful to study the behavior of the cavities under oligo-cyclic loading conditions[29,30]. In addition, with the cavity volume fraction V_{cav}^{SAXS} being very small (<<1), Equation (8) can be rewritten as follow:

$$2\pi^2\rho^2 V_{cav}^{SAXS} K_1 = \int_0^{\infty} I(q) q^2 \, dq \tag{9}$$

Again, the integral in the q-space is decomposed into 3 terms delimited by the 2 experimental extreme q-values: below q_1 ($0.05nm^{-1}$) linear extrapolation is applied; between q_1 and q_2 ($0.1nm^{-1}$) experimental data are processed; above q_2 the Porod's law is applied.

Figure 7 represents the volume fraction of the cavities V_{cav}^{SAXS} as a function of the applied axial nominal strain for all samples. For the quenched samples, having thinner crystalline lamellae and higher ST density, very little variation of V_{cav}^{SAXS} is observed upon loading suggesting that cavitation is not the driving structural phenomenon. Conversely, V_{cav}^{SAXS} shows significant hysteresis properties in isothermal samples. In the early stage of the first loading, prior to a critical strain ε_{onset}, no obvious evolution of cavitation is observed. ε_{onset} is graphically determined as the intersection of the two tangents (before and after cavity nucleation). Here, ε_{onset} equals 0.09 and 0.11 for the PE-A Isothermal and PE-B Isothermal samples respectively.

During unloading phase, V_{cav}^{SAXS} gradually decreases along a pathway differing from the loading one, with its minimum value at the zero-stress state being greater than the value observed during loading for the same macroscopic strain. The porosity can be thus partially decreased and it exhibits hysteretic behavior, which is in accordance with the finding of Addiego et al.[48]. During the consecutive loading steps, V_{cav}^{SAXS} evolution strongly differs from the first loading. Indeed, for stresses that have already been experienced by the sample, a gradual increase of V_{cav}^{SAXS} is observed with increasing strain. At any given strain, the value of V_{cav}^{SAXS} after N cycles is superior to the value after N-1 cycles, with the difference between the two decreasing as the number of cycles increases, suggesting eventual saturation. Therefore, throughout the oligo-cyclic tests, the volume fraction of the residual cavities accumulates at zero-stress state. Also, the hysteresis loops highlight that the evolution of cavities is time-dependent. Now comparing the different samples, the cavitation shows a great dependency on the microstructural properties: higher density of ST and thinner crystalline lamellae result in limited cavitation; this result is

emphasized through the comparison between the quenched and isothermal samples, but also when comparing the two isothermal samples. Indeed, the nucleation and accumulation of cavities are more pronounced in PE-A isothermal sample having thicker crystals and lower density of ST.

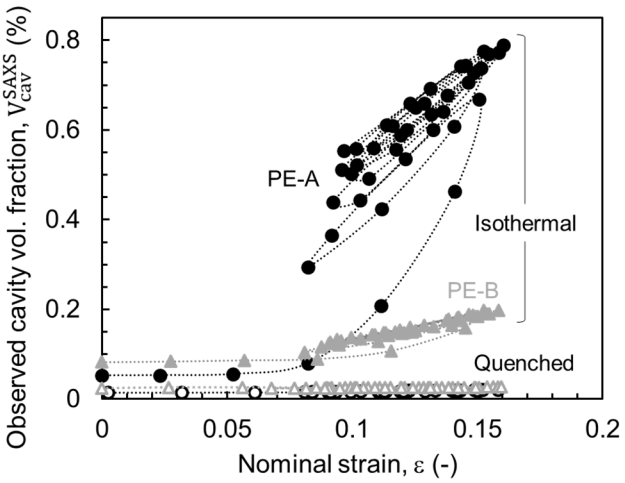

Figure 7: Evolution of the observed cavity volume fraction V_{cav}^{SAXS} as a function of the imposed nominal axial strain during oligo-cyclic test.

In the plastic regime, with the matrix deformation assumed to be isovolumetric, the macroscopic deformation ε_{vol} can be related to the volume fraction of cavities (the observed cavities generate only a part of the volumetric deformation $\varepsilon_{vol}^{SAXS} = V_{cav}^{SAXS}$). Also, the hydrostatic stress σ_H could be approximated by third of the axial nominal stress σ. The two quantities (ε_{vol}^{SAXS} and σ_H) are evaluated and plotted against one another in **Figure 8** for the PE-A isothermal sample. Hysteresis loops are clearly exhibited and can be related to the dissipated energy per unit volume attributed to the observed cavitation E_{cav}^{SAXS}.

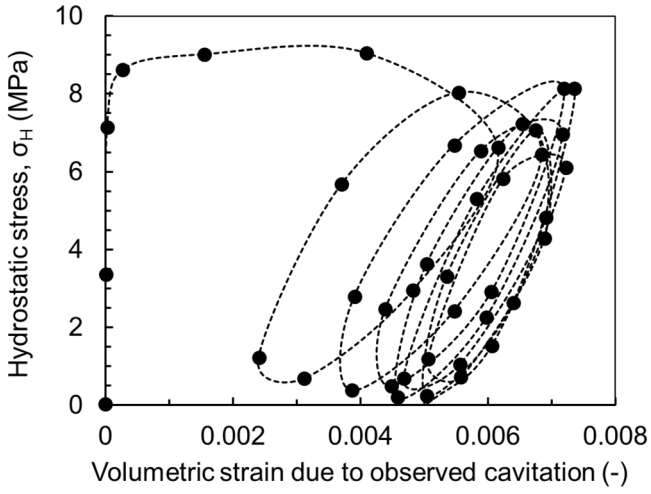

Figure 8: Hydrostatic stress as a function of the volumetric deformation due to observed cavities in PE-A Isothermal sample.

The total dissipated energy density (i.e. the energy dissipated per unit volume) occurring during the oligo-cyclic tests and denoted E_{total} is determined from the area of the hysteresis loops in the macroscopic nominal stress-strain curves (see **Figure 2**). Thus, the two dissipated energy densities E_{total} and E_{cav}^{SAXS} are presented in **Figure 9a** and **Figure 9b** respectively as a function of the cycle number for all materials.

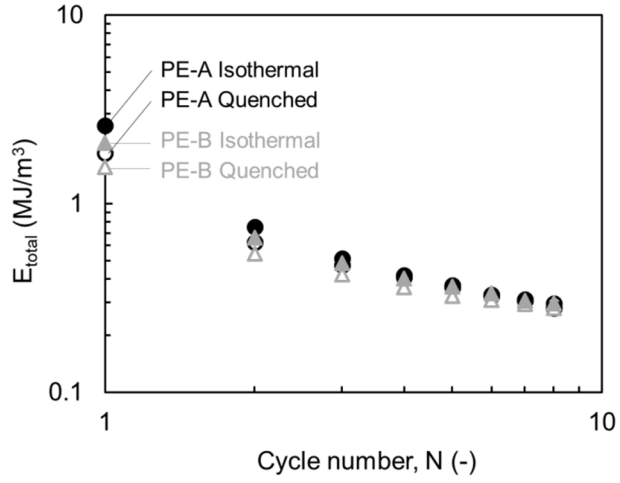

(a)

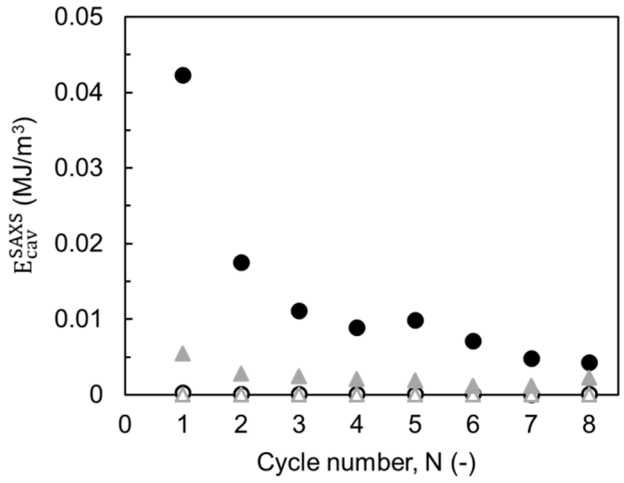

(b)

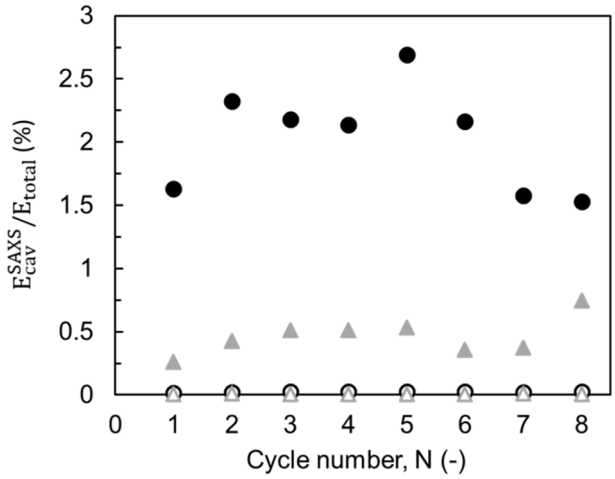

(c)

Figure 9: Energy profiles plotted as a function of the cycle number: (a) Total dissipated energy per unit volume E_{total}; (b) dissipated energy per unit volume due to cavitation E_{cav}^{SAXS}; (c) E_{cav}^{SAXS} / E_{total} ratio as a function of cycle number.

During the first load-unload cycle, ${}^{1}E_{total}$ shows a clear dependency on the microstructure: the sample with higher crystallinity exhibits a higher value of ${}^{1}E_{total}$. However, as the number of cycles increases, limited difference in ${}^{i}E_{total}$ (i>1) is observed, so that the dependency of E_{total} on the microstructure cannot be addressed. **Figure 9c** presents the corresponding E_{cav}^{SAXS}/E_{total} ratio as a function of the cycle number. The results show that the energy dissipated due to observed cavitation only accounts for a limited part of the total dissipated energy. The observed cavitation contribution reaches about only 3% in the PE-A isothermal sample, with the higher observed cavity volume fraction (see **Figure 7**). Therefore, the evolution of these observed nano-sized cavities does not dominate the energy dissipation taking place during the oligo-cyclic tensile tests.

Evolution of observed cavity dimension and shape

The evolution of the shape and associated dimensions of these observed cavities are also worth being discussed in parallel with their volume fraction to better understand and characterize the nucleation and growth of cavities under oligo-cyclic loading conditions. These dimensions are averaged over billions of nano-sized cavities.

A quantitative method proposed by Humbert et al.[29] is further applied to characterize such morphological evolutions in the isothermal samples. First, the scattering intensity can be decomposed as follow:

$$I(q) \propto F^2(q)S(q) \tag{10}$$

F(q) and *S(q)* are the shape and interference factors respectively. Assuming the cavities to be distant from each other, *S(q)* can be set equal to 1. Also, $F^2(q)$ can be decomposed in two orthogonal parts, parallel and perpendicular to the loading direction. With the elliptical cavities being assimilated to cylindrical objects, $F^2(q)$ becomes:

$$\mathrm{F^2(q)} = \left[\frac{\sin\left(\frac{1}{2}\mathrm{q_{\parallel}L}\right)}{\frac{1}{2}\mathrm{q_{\parallel}L}}\right]^2 \left[2\frac{\mathrm{J_1}\left(\frac{1}{2}\mathrm{q_{\perp}D}\right)}{\frac{1}{2}\mathrm{q_{\perp}D}}\right]^2 \tag{11}$$

$$\mathrm{q_{\parallel}} = \mathrm{q}\cos\gamma \tag{12}$$

$$\mathrm{q_{\perp}} = \mathrm{q}\sin\gamma \tag{13}$$

D is the diameter (perpendicular to the loading direction) *L* is the height (parallel to the loading direction) and γ is the angle between the normal of the base of the cylinder and the wave vector q, J_1 is the first order Bessel function. The two orthogonal contributions can be studied separately.

The calculation of *D* and *L* can be simplified using the following method: from the SAXS 2D patterns, the *I(q)-q²* profiles are obtained from the $\pm 5°$ azimuthal integration in the Zone H (corresponding to γ=90°) and Zone V (corresponding to γ=0°) . The radius of gyration R_0 could be calculated using Guinier's law described by equation (14) where $q \leq 0.1nm^{-1}$. *D* and *L* are finally approximated by the spherical diameter D_{sp} using relation (15).

$$\mathrm{I(q)} = \mathrm{I(0)e^{\left(-\frac{R_0^2 q^2}{3}\right)}} \tag{14}$$

$$\mathrm{D_{sp}} = 2 \times \frac{\mathrm{R_0}}{\sqrt{\frac{3}{5}}} \tag{15}$$

The average cavity dimensions are presented in **Figure 10** as a function of the macroscopic strain.

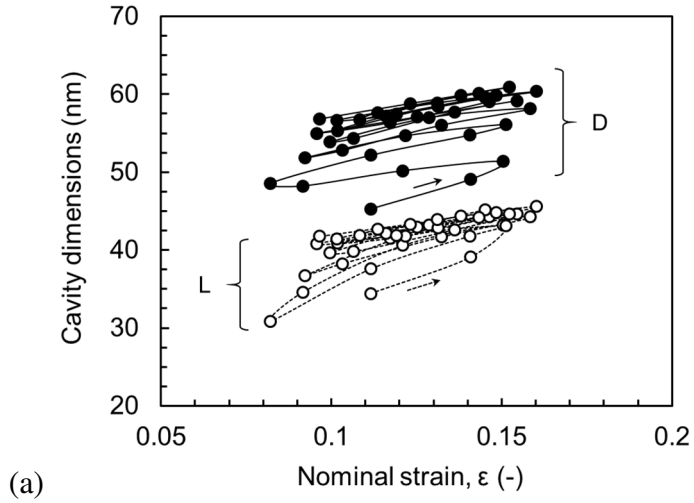

(a)

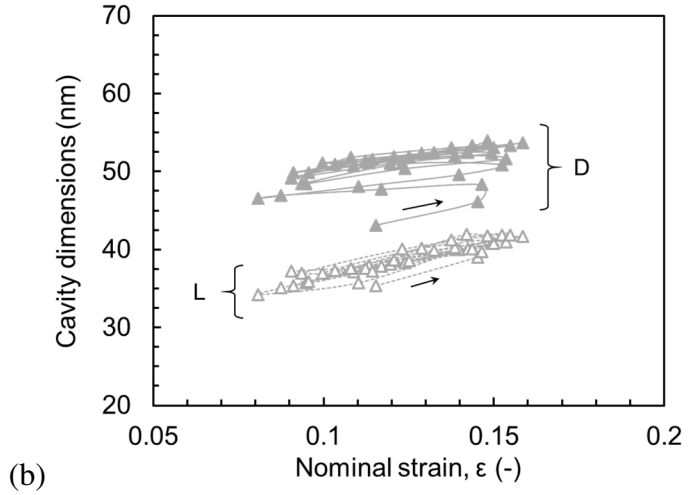

(b)

Figure 10: Evolution of the cavity dimensions:
(a) PE-A Isothermal sample; (b) PE-B Isothermal sample.

The first estimation of the initial cavity dimensions in both PE-A and PE-B isothermal samples are obtained after nucleation during the first loading step. D=45 nm and L=35 nm are found. In the two samples, it worth noting that initial L values are larger than the thickness of a single amorphous layer, meaning that the onset of the cavity nucleation is not captured by SAXS as it is almost instantaneous[29,30]. The cavitation is considered to be firstly induced in the equatorial region of spherulite[9,36,37,49,58], the oriented crystalline lamellae in this region should strongly contribute to the limitation of cavity growth along tensile direction.

With additional stretching, the cavities begin to grow along both directions. In the literature, during uniaxial tensile stretching, the initial oblate cavities will further transform into the prolate one (L>D) accompanied with the fibrillary transformation at large strain[29,36,37,59]. These prolate cavities are located in the inter-fibrillary region, where the lateral propagation is limited thanks to the shish crystalline blocks within the microfibrils [36,60].

However, in our case, the overall spherulitic structure remains: despite the occurrence of fragmentation of lamellae, the growth of cavity in the equatorial region is still limited along the tensile direction thanks to the remaining lamellae. Therefore, the cavity dimension increases mainly along the direction perpendicular to the loading direction (D).

According to our measurement, upon unloading, the decrease is also more pronounced and rapid along the tensile direction (L) implying that the cavities tend to close primarily along the macroscopic loading direction. The cavities are not entirely closed at zero stress and the slight decrease of D should be related to the closure of the cavity tips. Taking PE-B isothermal sample as an example, **Figure 11a** summarizes the cavity's shape evolution throughout the test and **Figure 11b** and **c** focus on noticeable deformed states.

At the end of an oligo-cyclic test, the cavities in PE-A isothermal sample are in average larger than the ones in the PE-B isothermal sample with both *D* and *L* being greater. Previous results showed that the observed cavity volume fraction of PE-A isothermal sample is about 4 times higher than that of the PE-B isothermal sample (see **Figure 7**).

However, the difference in dimension is much smaller, implying that the amount of cavities in PE-A isothermal sample should also be higher in this q window. Assuming that the cavities are ellipsoid in shape, the average volume of the observed cavities, denoted A, could be estimated using relation (16):

$$A = \frac{4}{3} \times \pi \times D^2 \times L \qquad (16)$$

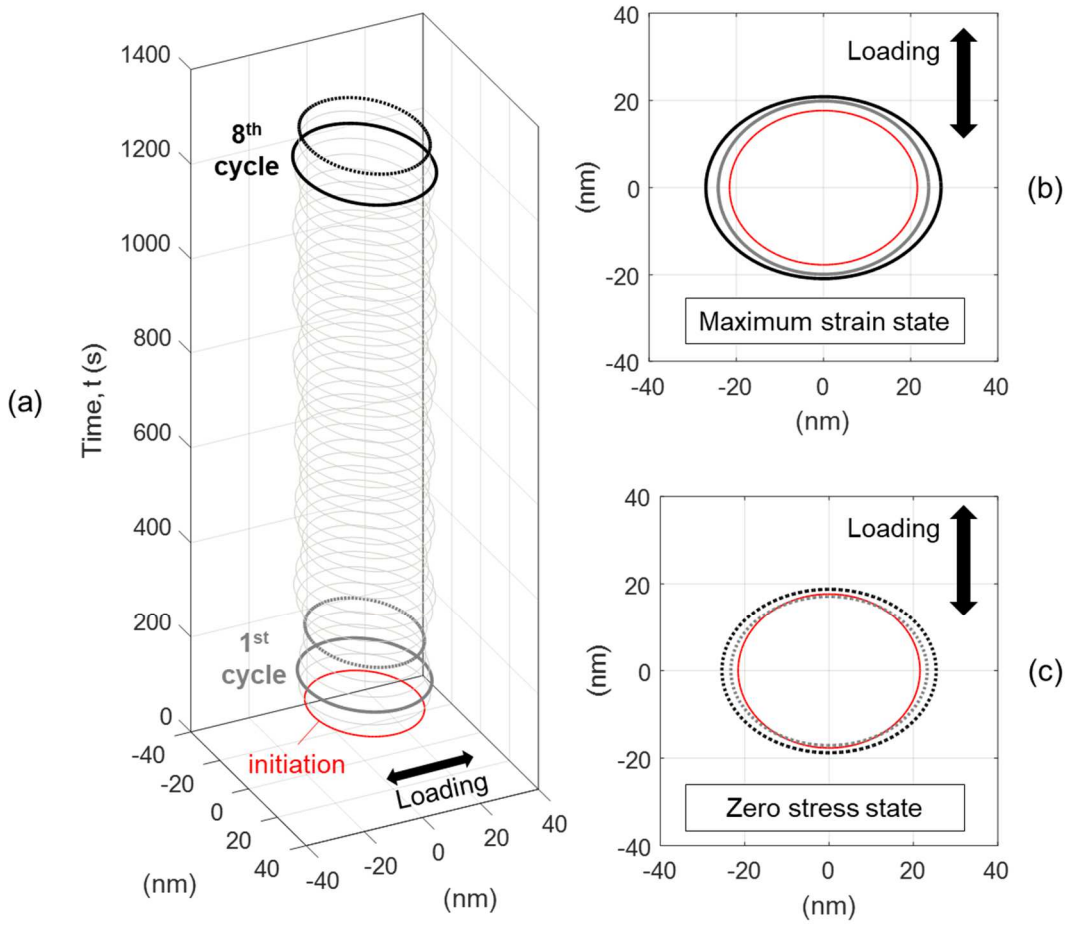

Figure 11: Evolution of cavities under oligo-cyclic loading conditions (PE-B Isothermal sample): (a) time evolution; (b) maximum-strain state (loading); (c) zero-stress state (unloading).

The relative volume variation induced by the evolution of the cavity sizes could then be estimated. Moreover, according to the evolution of V_{cav}^{SAXS}, the relative volume variation of observed cavities induced by both the varying number of cavities and their growth (change of dimension) could be calculated. **Figure 12** compares the volume variation of a unit average cavity and the total cavities at zero-stress states as a function of the cycle number.

After the first cycle (nucleation), the relative volume variation of the observed cavities is considered to be 0. According to the results, at any given time, the relative volume variations of the cavities and the total number of observed cavities are about the same in both isothermal samples. This phenomenon indicates that after the first cycle, the subsequent evolution of the observed cavity volume fraction could be mainly attributed to the opening and closure of the previously nucleated cavities rather than the nucleation of new cavities.

Also, the "saturation" of the cavity dimension only suggests that the growth rate is significantly decreased within the following cycles (after the first few cycles). The lateral growth is mitigated

by the stress transmitters, which are already strongly taut around the cavity. Also, it can be supposed that the remaining cycles mainly induce visco-elastic fatigue effects. Indeed, another study suggested that the further increase of D was related to the fatigue failure of semi-crystalline polymers[49].

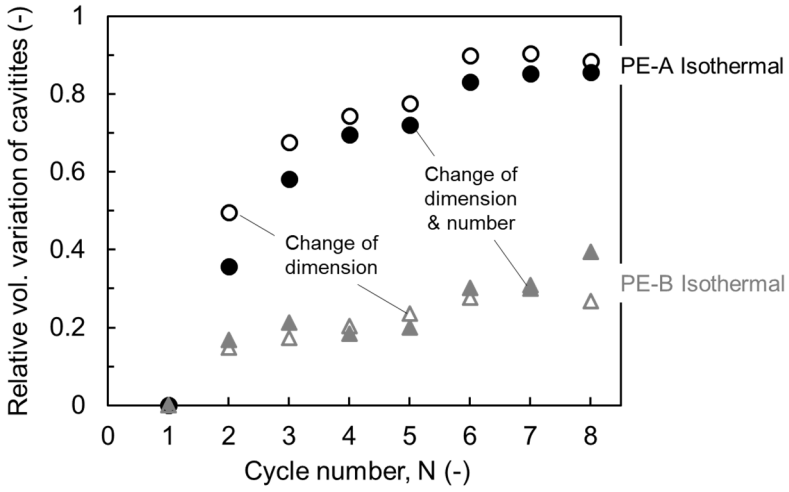

Figure 12: Variation of unit/total cavity volume at zero stress states as a function of the cycle number.

Figure 13 confronts the evolution of the aspect ratio (*D/L*) of these cavities along with the applied macroscopic axial strain of PE-B isothermal sample with respect to time: the aspect ratio (*D/L*) is seen to remain superior to unity at any given time confirming the elliptical shape of the cavities. Upon cycling, the aspect ratio reaches its minimum at the end of the loading steps and its maximum when the sample is fully unloaded. As time (and thus number of cycles) goes, the aspect ratio at zero-stress states increases progressively from 1.2 to 1.3, evidencing that the cavities become more and more elliptical as a consequence of the propagation of cavities along the direction perpendicular to the loading axis.

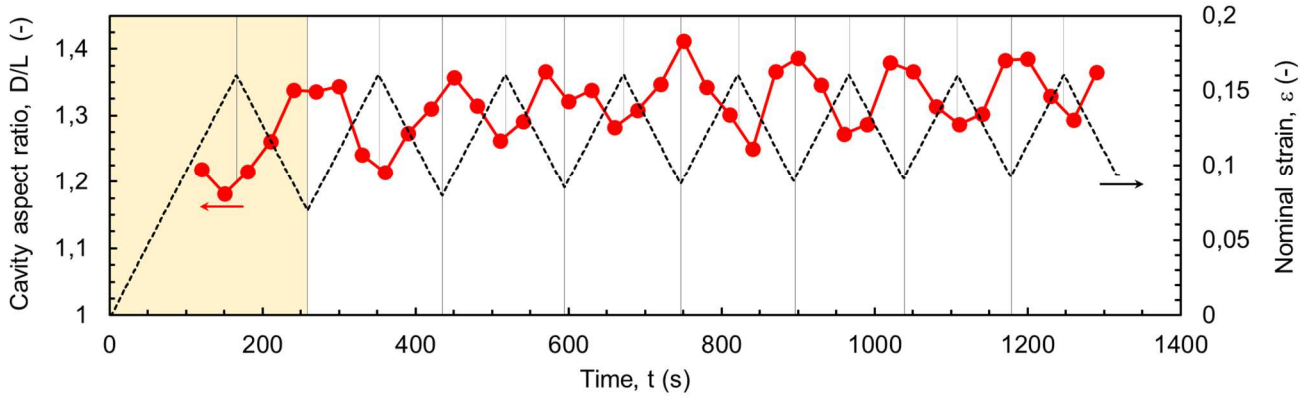

Figure 13: Time evolution of the cavity aspect ratio and applied nominal strain in the PE-B Isothermal sample under mixed-mode oligo-cyclic test.

Conclusion

Under mixed mode oligo-cyclic tensile loading conditions, meso- and micro- structural evolutions are shown in different HDPE samples obtained from varying thermal treatments. According to the macroscopic observation, the mechanical response strongly differs between the first and the consecutive loading cycles of the oligo-cyclic test. *In-situ* SAXS measurements allowed evidencing that: i) the deformations of nano-sized lamellar stacks located at the equatorial region of micron-sized spherulites remain proportional to the macroscopic ones. In addition, within this region of the spherulites, the first cycle induces the most important shearing/fragmentation of the crystallites and the remaining cycles cause the accumulating evolution and stabilization of the crystalline structure. ii) nano-sized cavities were observed in the isothermal samples, these micro-voids were nucleated during the first loading step, and partially closed upon the first unloading step. More importantly, with consecutive cycles, only the dimensions of the cavities evolve whereas no additional nucleation appears in the observation window. These cavities were found to grow primarily perpendicular to the loading/unloading direction. Focusing on the zero-stress states at each cycle, the initiated cavities progressively grew up to a saturated size. These results reveal that the oligo-cyclic tests cause significant structural evolutions during the first few cycles (especially the first one). Within the consecutive loading cycles, the stabilizing microstructure and the associated macroscopic mechanical behavior suggest that the additional loading-unloading processes mainly induce visco-elastic fatigue effects as the continuing accumulation of the initiated microstructure evolutions. Moreover, these structural evolutions (initiation-accumulation-stabilization) also suggest that the origin of the macroscopic Mullins behavior could be complex as several mechanisms could potentially interfere (plasticity, cavitation, phase transformation etc.). Ongoing investigations using in-situ SAXS measurements for varying maximum strains and applied to a larger range of microstructures should be helpful to better understand this complex phenomenon.

Also, the tendency for the PE to “cavitate” was highly dependent on the initial microstructure, as it was limited in quenched samples due to their high density of stress transmitters, lower crystallinity and thinner crystallites. This difference of cavitation behavior in these samples should be valuable for the further investigation on the origin of the dependency of the mechanical losses during oligo-cyclic deformation in HDPE materials on their pristine microstructures/morphologies so that it can make contribution to the design and selection of HDPE materials of pipeline systems combined with other mechanical evaluations.

Acknowledgments

The authors are indebted to French SOLEIL synchrotron for time allocation on the SWING beamline, INEOS (Brussels, Belgium) for supplying the PE pellets and the GPC characterizations, EDF Research &Development and EDF DIPNN Design and Technology branch for the grant of a doctoral fellowship to H.GUO.

References

[1] W.W. Chen, B. Shih, Y. Chen, J. Hung, H. H. Hwang, Seismic response of natural gas and water pipelines in the Ji-Ji earthquake, Soil Dyn. Earthq. Eng. 22 (2002) 1209–1214.

[2] T. H. Abdoun, D. Ha, Michael J. O'Rourke, M. D. Symans, T. D. O'Rourke, M. C. Palmer, H. E. Stewart, Factors influencing the behavior of buried pipelines subjected to earthquake faulting, Soil Dyn. Earthq. Eng. 29 (2009) 415–427.

[3] D. Ha, T. H. Abdoun, M. J. O'Rourke, M. D. Symans, T. D. O'Rourke, M. C. Palmer, H. E. Stewart, Centrifuge modeling of earthquake effects on buried high-density polyethylene (HDPE) pipelines crossing fault zones, J. Geotech. Geoenvironmental Eng. 134 (2008) 1501–1515.

[4] A. Masi, G. Santarsiero, D. Nigro, Cyclic tests on external RC beam-column joints: role of seismic design level and axial load value on the ultimate capacity, J. Earthq. Eng. 17 (2013) 110–136.

[5] P. Cassese, P. Ricci, G. M. Verderame, Experimental study on the seismic performance of existing reinforced concrete bridge piers with hollow rectangular section, Eng. Struct. 144 (2017) 88–106.

[6] V. Ji, Y. Zhang, C. Chen, The non-destructive estimation of the superficial mechanical properties of components in the INCONEL 600 alloy by X-ray diffraction peak width, Surf. Coat. Technol. 130 (2000) 95–99.

[7] M. J. W Kanters, T. Kurokawa, L. E. Govaert, Competition between plasticity-controlled and crack-growth controlled failure in static and cyclic fatigue of thermoplastic polymer systems, Polym. Test. 50 (2016) 101–110.

[8] R. P.M Janssen, L. E. Govaert, H. E. H Meijer, An analytical method to predict fatigue life of thermoplastics in uniaxial loading: sensitivity to wave type, frequency, and stress amplitude, Macromolecules. 41 (2008) 2531–2540.

[9] E. Mourglia-Seignobos, D. R. Long, L. Odoni, L. Vanel, P. Sotta, C. Rochas, Physical mechanisms of fatigue in neat polyamide 6, 6, Macromolecules. 47 (2014) 3880–3894.

[10] S. T. T. Nguyen, S. Castagnet, J.C. Grandidier, Nonlinear viscoelastic contribution to the cyclic accommodation of high density polyethylene in tension: Experiments and modeling, Int. J. Fatigue. 55 (2013) 166–177.

[11] L. Mullins, Permanent set in vulcanized rubber, Rubber Chem. Technol. 22 (1949) 1036–1044.

[12] L. Mullins, Softening of rubber by deformation, Rubber Chem. Technol. 42 (1969) 339–362.

[13] J. Diani, B. Fayolle, P. Gilormini, A review on the Mullins effect, Eur. Polym. J. 45 (2009) 601–612.

[14] A. D. Drozdov, Mullins' effect in semicrystalline polymers, Int. J. Solids Struct. 46 (2009) 3336–3345.

[15] M. Makki, G. Ayoub, H. Abdul-Hameed, F. Zaïri, B. Mansoor, M. Naït-Abdelaziz, M. Ouederni, Mullins effect in polyethylene and its dependency on crystal content: a network alteration model, J. Mech. Behav. Biomed. Mater. 75 (2017) 442–454.

[16] M. Wang, J. Shen, J. Li, S. Guo, Network alteration theory on Mullins effect in semicrystalline polymers, Polym. Int. 64 (2015) 105–112.

[17] S. Govindjee, J. Simo, A micro-mechanically based continuum damage model for carbon black-filled rubbers incorporating Mullins' effect, J. Mech. Phys. Solids. 39 (1991) 87–112.

[18] R. Houwink, Slipping of molecules during the deformation of reinforced rubber, Rubber Chem. Technol. 29 (1956) 888–893.

[19] D. E. Hanson, M. Hawley, R. Houlton, K. Chitanvis, P. Rae, E. B. Orler, D. A. Wrobleski, Stress softening experiments in silica-filled polydimethylsiloxane provide insight into a mechanism for the Mullins effect, Polymer. 46 (2005) 10989–10995.

[20] G. Ayoub, F. Zaïri, M. Naït-Abdelaziz, J. M. Gloaguen, Modeling the low-cycle fatigue behavior of visco-hyperelastic elastomeric materials using a new network alteration theory: application to styrene-butadiene rubber, J. Mech. Phys. Solids. 59 (2011) 473–495.

[21] S. Humbert, O. Lame, J. M. Chenal, C. Rochas, G. Vigier, Small strain behavior of polyethylene: in situ SAXS measurements, J. Polym. Sci. Part B Polym. Phys. 48 (2010) 1535–1542.

[22] B. Xiong, O. Lame, J. M. Chenal, C. Rochas, R. Seguela, G. Vigier, In-situ SAXS study of the mesoscale deformation of polyethylene in the pre-yield strain domain: Influence of microstructure and temperature, Polymer. 55 (2014) 1223–1227.

[23] K. Nitta, A molecular theory of stress–strain relationship of spherulitic materials, Comput. Theor. Polym. Sci. 9 (1999) 19–26.

[24] Y. Men, Critical Strains Determine the Tensile Deformation Mechanism in Semicrystalline Polymers, ACS Publications, 2020.

[25] Y. Men, G. Strobl, Critical strains determining the yield behavior of s-PP, J. Macromol. Sci. Part B. 40 (2001) 775–796.

[26] L. Lin, A. S. Argon, Structure and plastic deformation of polyethylene, J. Mater. Sci. 29 (1994) 294–323.

[27] R. Hiss, S. Hobeika, C. Lynn, G. Strobl, Network stretching, slip processes, and fragmentation of crystallites during uniaxial drawing of polyethylene and related copolymers. A comparative study, Macromolecules. 32 (1999) 4390–4403.

[28] F. Addiego, A. Dahoun, C. G'Sell, J. M. Hiver, O. Godard, Effect of microstructure on crazing onset in polyethylene under tension, Polym. Eng. Sci. 49 (2009) 1198–1205.

[29] S. Humbert, O. Lame, J. M. Chenal, C. Rochas, G. Vigier, New insight on initiation of cavitation in semicrystalline polymers: in-situ SAXS measurements, Macromolecules. 43 (2010) 7212–7221.

[30] B. Xiong, O. Lame, J. M. Chenal, C. Rochas, R. Seguela, G. Vigier, In-situ SAXS study and modeling of the cavitation/crystal-shear competition in semi-crystalline polymers: Influence of temperature and microstructure in polyethylene, Polymer. 54 (2013) 5408–5418.

[31] B. Xiong, O. Lame, J. M. Chenal, Y. Men, R. Seguela, G. Vigier, Critical stress and thermal activation of crystal plasticity in polyethylene: Influence of crystal microstructure and chain topology, Polymer. 118 (2017) 192–200.

[32] K. Nitta, M. Takayanagi, Novel proposal of lamellar clustering process for elucidation of tensile yield behavior of linear polyethylenes, J. Macromol. Sci. Part B. 42 (2003) 107–126.

[33] Y. Men, J. Rieger, G. Strobl, Role of the entangled amorphous network in tensile deformation of semicrystalline polymers, Phys. Rev. Lett. 91 (2003) 095502.

[34] Y. Wang, Z. Jiang, L. Fu, Y. Lu, Y. Men, Lamellar thickness and stretching temperature dependency of cavitation in semicrystalline polymers, PLoS One. 9 (2014).

[35] M. F. Butler, A. M. Donald, A real-time simultaneous small-and wide-angle X-ray scattering study of in situ polyethylene deformation at elevated temperatures, Macromolecules. 31 (1998) 6234–6249.

[36] A. Pawlak, A. Galeski, Cavitation during tensile drawing of annealed high density polyethylene, Polymer. 51 (2010) 5771–5779.

[37] T.F. Morgeneyer, H. Proudhon, P. Cloetens, W. Ludwig, Q. Roirand, L. Laiarinandrasana, E. Maire, Nanovoid morphology and distribution in deformed HDPE studied by magnified synchrotron radiation holotomography, Polymer. 55 (2014) 6439–6443.

[38] N. Selles, P. Cloetens, H. Proudhon, T.F. Morgeneyer, O. Klinkova, N. Saintier, L. Laiarinandrasana, Voiding mechanisms in deformed polyamide 6 observed at the nanometric scale, Macromolecules. 50 (2017) 4372–4383.

[39] M.F. Butler, A.M. Donald, W. Bras, G.R. Mant, G.E. Derbyshire, A.J. Ryan, A real-time simultaneous small-and wide-angle X-ray scattering study of in-situ deformation of isotropic polyethylene, Macromolecules. 28 (1995) 6383–6393.

[40] M.F. Butler, A.M. Donald, A.J. Ryan, Time resolved simultaneous small-and wide-angle X-ray scattering during polyethylene deformation 3. Compression of polyethylene, Polymer. 39 (1998) 781–792.

[41] B. Xiong, O. Lame, J. M. Chenal, C. Rochas, R. Seguela, On the strain-induced fibrillar microstructure of polyethylene: Influence of chemical structure, initial morphology and draw temperature, Express Polym. Lett. 10 (2016) 311.

[42] Z. Jiang, Y. Tang, J. Rieger, H. F. Enderle, D. Lilge, S.V. Roth, R. Gehrke, W. Heckmann, Y. Men, Two lamellar to fibrillar transitions in the tensile deformation of high-density polyethylene, Macromolecules. 43 (2010) 4727–4732.

[43] S. André-Castagnet, S. Tencé-Girault, Relationships between mechanical tensile behavior and micro-mechanisms in poly (vinylidene fluoride) at high temperatures: Influence of the molecular weight distribution, J. Macromol. Sci. Part B. 41 (2002) 957–976.

[44] G. Strobl, Crystallization and melting of bulk polymers: New observations, conclusions and a thermodynamic scheme, Prog. Polym. Sci. 31 (2006) 398–442.

[45] G. Strobl, The physics of polymers, Springer, 1997.

[46] Y. Men, G. Strobl, From crystalline block slips to dominance of network stretching- Mechanisms of tensile deformation in semi-crystalline polymers, Chin. J. Polym. Sci. 20 (2002) 161–170.

[47] S. Tencé-Girault, S. Lebreton, O. Bunau, P. Dang, F. Bargain, Simultaneous SAXS-WAXS experiments on semi-crystalline polymers: Example of PA11 and its brill transition, Crystals. 9 (2019) 271.

[48] F. Addiego, S. Patlazhan, K. Wang, S. André, Sigrid Bernstorff, David Ruch, Time-resolved small-angle X-ray scattering study of void fraction evolution in high-density polyethylene during stress unloading and strain recovery, Polym. Int. 64 (2015) 1513–1521.

[49] I. Raphael, N. Saintier, G. Robert, J. Béga, L. Laiarinandrasana, On the role of the spherulitic microstructure in fatigue damage of pure polymer and glass-fiber reinforced semi-crystalline polyamide 6.6, Int. J. Fatigue. 126 (2019) 44–54.

[50] R.P. Janssen, D. de Kanter, L.E. Govaert, H.E. Meijer, Fatigue life predictions for glassy polymers: a constitutive approach, Macromolecules. 41 (2008) 2520–2530.

[51] S. Toki, Igors Sics, C. Burger, D. Fang, L. Liu, B.S. Hsiao, S. Datta, A.H. Tsou, Structure Evolution during Cyclic Deformation of an Elastic Propylene-Based Ethylene– Propylene Copolymer, Macromolecules. 39 (2006) 3588–3597.

[52] A. Alizadeh, L. Richardson, J. Xu, S. McCartney, H. Marand, Y. W. Cheung, S. Chum, Influence of structural and topological constraints on the crystallization and melting behavior of polymers. 1. Ethylene/1-octene copolymers, Macromolecules. 32 (1999) 6221–6235.

[53] L. Hubert, L. David, R. Séguéla, G. Vigier, Small-angle X-ray scattering investigation of the deformation processes in the amorphous phase of high density polyethylene, Polym. Int. 53 (2004) 582–585.

[54] S. Humbert, O. Lame, G. Vigier, Polyethylene yielding behaviour: What is behind the correlation between yield stress and crystallinity?, Polymer. 50 (2009) 3755–3761.

[55] B. Crist, C. J. Fisher, Paul R. Howard, Mechanical properties of model polyethylenes: tensile elastic modulus and yield stress, Macromolecules. 22 (1989) 1709–1718.

[56] B. Xiong, O. Lame, J. M. Chenal, C. Rochas, R. Seguela, G. Vigier, Amorphous phase modulus and micro–macro scale relationship in polyethylene via in situ SAXS and WAXS, Macromolecules. 48 (2015) 2149–2160.

[57] M. Krumova, S.Henning, G. H. Michler, Chevron morphology in deformed semicrystalline polymers, Philos. Mag. 86 (2006) 1689–1712.

[58] S. Castagnet, S. Girault, J. L. Gacougnolle, P. Dang, Cavitation in strained polyvinylidene fluoride: mechanical and X-ray experimental studies, Polymer. 41 (2000) 7523–7530.

[59] A. Blaise, C. Baravian, J. Dillet, L.J. Michot, S. André, Characterization of the mesostructure of HDPE under “in situ” uniaxial tensile test by incoherent polarized steady-light transport, J. Polym. Sci. Part B Polym. Phys. 50 (2012) 328–337.

[60] J. M. Brady, E. L. Thomas, Deformation of oriented high density polyethylene shish-kebab films, J. Mater. Sci. 24 (1989) 3311–3318.